catalysts

MDPI

Article

BiOI-MIL Binary Composite for Synergistic Azo Dye AR14 Discoloration

Mahmoud Shams [1,2], Samane Abd Mojiri [3], Masoomeh Shafaee [4], Najmaldin Ezaldin Hassan [5], Aliakbar Dehghan [1,2], Mansour Baziar [6], Elaheh K. Goharshadi [7] and Shahabaldin Rezania [8,*]

1 Social Determinants of Health Research Center, Mashhad University of Medical Sciences, Mashhad 9177948564, Iran; shamsmh@mums.ac.ir (M.S.); dehghanaa@mums.ac.ir (A.D.)
2 Department of Environmental Health Engineering, School of Health, Mashhad University of Medical Sciences, Mashhad 9177948564, Iran
3 Student Research Committee, Department of Environmental Health Engineering, School of Health, Mashhad University of Medical Sciences, Mashhad 9177948564, Iran; samane.am74@gmail.com
4 Department of Physical Chemistry, School of Chemistry, University College of Science, University of Tehran, Tehran 14155, Iran; ma.sh36163@gmail.com
5 College of Engineering, Civil and Environment Department, University of Zakho, Duhok 42001, Iraq; najmaldin.hassan@uoz.edu.krd
6 Department of Environmental Health Engineering, Ferdows Faculty of Medical Sciences, Birjand University of Medical Sciences, Birjand 9717853577, Iran; baziar.ehe@gmail.com
7 Department of Chemistry, Faculty of Science, Ferdowsi University of Mashhad, Mashhad 9177948974, Iran; gohari@um.ac.ir
8 Department of Environment and Energy, Sejong University, Seoul 05006, Republic of Korea
* Correspondence: shahab.rezania@sejong.ac.kr

Abstract: Acid red 14 (AR14) is a widely used azo dye that belongs to a major family of commercial dyes employed extensively in the textile industry. The present study aimed to investigate the photocatalytic discoloration of AR14 using a visible-light-responsive catalyst. The composite catalyst was synthesized by integrating thermally modified MIL-101 (M-MIL) integrated into bismuth oxide. Thermal modification of MIL-101 produced octahedral α-Fe_2O_3 particles with a size of 1–2 µm, which were incorporated into bismuth oxyiodide (BiOI) featuring a nanosheet structure. BiOI@M-MIL composite exhibited an enhanced photocatalytic activity. The bandgap energy, E_g, of BiOI was reduced from 1.95 eV to 1.73 eV in the composite. Photocatalytic reactions were performed under visible-light irradiation using a 5 W cold LED lamp. The AR14 discoloration tests demonstrated that BiOI@M-MIL was 1.81-fold more efficient compared to pristine BiOI. Key parameters affecting AR14 discoloration —such as catalyst dosage, pH, dye concentration, and contact time, were investigated. The composite achieved almost a complete dye removal efficiency of 94.26% under experimental conditions. Radical trapping tests highlighted the crucial role of superoxide radicals, O_2^-, in the dye discoloration process. BiOI@M-MIL takes advantage of simultaneous adsorption and photocatalysis with the highest adsorption capacity of 45.32 mg g^{-1} and 32.2 mg g^{-1}, based on Sips and Langmuir models, respectively. The catalyst also showed good reusability and ~14% loss in removal efficiency after five consecutive cycles. In conclusion, the BiOI@M-MIL composite demonstrates excellent photocatalytic performance, combining low energy consumption with material stability, making it a promising candidate for AR14 discoloration.

Keywords: photocatalysis; acid red 14 (AR14); Nano composite; bismuth-based catalysts; metal organic framework

check for updates

Academic Editor: Bo Weng

Received: 7 November 2024
Revised: 20 December 2024
Accepted: 27 December 2024
Published: 30 December 2024

Citation: Shams, M.; Abd Mojiri, S.; Shafaee, M.; Hassan, N.E.; Dehghan, A.; Baziar, M.; Goharshadi, E.K.; Rezania, S. BiOI-MIL Binary Composite for Synergistic Azo Dye AR14 Discoloration. *Catalysts* **2025**, *15*, 26. https://doi.org/10.3390/catal15010026

Copyright: © 2024 by the authors. Licensee MDPI, Basel, Switzerland. This article is an open access article distributed under the terms and conditions of the Creative Commons Attribution (CC BY) license (https://creativecommons.org/licenses/by/4.0/).

1. Introduction

The textile industry is a significant contributor to global water and environmental pollution [1–3]. Azo dyes pose a particular challenge due to their complex structures and resistance to conventional wastewater treatment methods [4–7]. Acid Red 14 (AR14) is an extensively used azo dye that presents a remarkable environmental threat [8]. The persistence of AR14 arises from the complex aromatic structures and strong chromophores within AR14 molecules, rendering them resistant to biodegradation and posing potential environmental threats. Its presence in water bodies disrupts aquatic ecosystems by reducing light penetration, hindering photosynthesis, and potentially exhibiting toxic effects on organisms [9–11].

Developing efficient and sustainable methods for degrading azo dyes like AR14 is essential for mitigating textile wastewater pollution. Photocatalysis has emerged as a promising approach due to its ability to utilize light irradiation to activate catalysts and generate reactive species, including hydroxyl radicals ($OH^{\cdot}$) and superoxide radicals ($O_2^{\cdot -}$), to degrade pollutants [12]. These radicals effectively split the complex structures of organic pollutants, leading to their mineralization into harmless components [13,14].

Metal–organic frameworks (MOFs), a class of highly porous materials with tunable structures, large surface area, defined pore architectures, and the ability to incorporate various metal centers, have attracted considerable interest as photocatalysts for efficient dye degradation [15–18]. However, a major limitation of pristine MOFs in photocatalysis is the high recombination rate of photogenerated electron hole pairs. This recombination reduces the efficiency of radical generation, hindering the degradation process [19]. To improve the photocatalytic performance of MOFs, the incorporation of a semiconductor with a suitable band gap for visible light absorption has been offered [20].

Of bismuth-based catalysts, bismuth oxyiodide (BiOI) demonstrates excellent light harvesting properties and efficient charge separation [21–23]. However, like other pure semiconductors, BiOI suffers from inherent drawbacks, including low surface area, lack of surface-active sites, and rapid recombination rates for the electron holes [24–26]. The integration of MOFs with BiOI proposes a synergistic approach to overcome the limitations of each material [27,28]. MOFs provide a large surface area for dye adsorption and improve light absorption, while BiOI promotes efficient charge separation and generation of reactive species [27,29]. Since the MOF matrix can suppress the recombination of electron hole pairs in BiOI, the generation of reactive species enhances pollutant degradation. The favorable contact between BiOI and the MOF framework facilitates efficient charge transfer, minimizing recombination and enhancing photocatalytic activity [30].

Several researchers have investigated MOF-BiOI composites for the photocatalytic degradation of various organic pollutants. For instance, Islam et al. [30] synthesized BiOI nanoparticles decorated on MIL-88B(Fe) and demonstrated its efficient degradation of colorless phenol and ciprofloxacin (CIP) under visible light irradiation. Liang et al. [31] fabricated a ternary heterojunction BiOI@UIO-66(NH_2)@g-C_3N_4 photocatalyst to degrade Rhodamine B and Tetracycline (TC). Similarly, Dai et al. [32] reported the development of a MIL-125-NH_2@BiOI composite exhibiting superior photocatalytic activity for the degradation of Cr (VI) and TC. Khasevani et al. [33] prepared binary and ternary composites of BiOI with NH_2-MIL-101(Fe) as photocatalysts for the removal of CIP from water sources.

Here, we developed a sustainable catalyst by integrating MOF with BiOI to efficiently abate AR14 under visible light irradiation. The materials were fully characterized, and the adsorptive and catalytic performance of pristine BiOI was compared to that of the novel composite. Dye discoloration under visible light irradiation was investigated as a function of irradiation time, catalyst dose, pH, and dye concentration. Kinetic study and radical trapping tests were performed to analyze the mechanisms involved in the dye removal.

Also, the reusability of material was assessed by application of BiOI@M-MIL in consecutive use–reuse cycles. Therefore, this work attempts the integration of MIL-101 derived α-Fe_2O_3 to BiOI to develop BiOI@M-MIL for the first time. This is a novel synthesis approach resulting in a material that outperforms pristine BiOI catalytic performance. Owing to the demands for developing sustainable materials outlined in the literature [34] the new composite performance perfectly aligns with the eco-friendly principles.

2. Results and Discussion

2.1. Characterization of Materials

The crystalline structure and phase components of BiOI, M-MIL, and BiOI@M-MIL were analyzed using X-ray diffraction (XRD) patterns that are presented in Figure 1. In the XRD pattern of M-MIL, the diffraction peaks at 2θ = 24.1, 33.1, 35.6, 40.8, 49.5, 54.1, 57.5, 62.4, and 64° are agreed with (012), (104), (110), (113), (024), (116), (018), (214), and (300) crystalline planes [35]. XRD pattern of BiOI@M-MIL includes extra peaks related to (100), (200), (110), (210), (011), (111), (211), (400), (020), (411), (211), and (022) crystalline planes of BiOI [36]. Moreover, the peaks at 2θ = 29.7 and 37.4° prove the synthesis of BiOI on a BiOI@M-MIL substrate successfully.

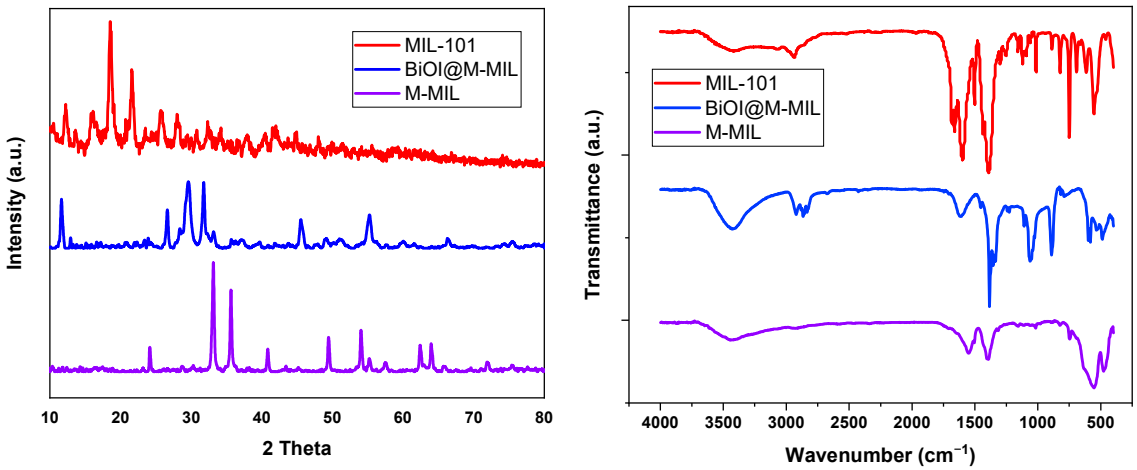


Figure 1. The X-ray diffraction (XRD) and FTIR spectra of patterns for MIL-101, M-MIL, and BiOI@M-MIL.

Surface functional groups of M-MIL and BiOI@M-MIL were identified by furrier transform infrared (FTIR) spectrometry. Figure 1 also shows FTIR spectra of MIL-101, BiOI@M-MIL, and BiOI@M-MIL between 400–4000 cm^{-1} wavenumbers. As shown in the figure, a vibration band within the 3400–3700 cm^{-1} range is agreed to the stretching mode of hydroxyl groups (–OH). In the FTIR spectrum of BiOI@M-MIL, the chemical bands at 235.9 and 2840 cm^{-1} are related to asymmetric and symmetric stretching vibrations of C-H, respectively. The chemical band at 1661.1 cm^{-1} is due to the vibration of the C=O band. The chemical bands at 1391.34 and 1598.8 cm^{-1} are attributed to symmetric and asymmetric vibrations of carboxylic groups (COO^-), respectively. The bands at 749.86, 1017.8, and 1157.23 cm^{-1} are associated with the bending vibrations of C–H. The band that appeared at 1502.68 cm^{-1} corresponds to C=C vibrations in the benzene rings [37]. The band at 554.25 cm^{-1} indicates the stretching vibration of Fe–O, while the bands at 553.2 and 477.48 cm^{-1} represent the stretching vibration of Fe–O within –Fe_2O_3 [37]. The weak bands at 1393.89 and 1550.93 cm^{-1} can be attributed to BiOI@M-MIL in –Fe_2O_3. In the FTIR spectrum of BiOI@M-MIL photocatalyst, not only the chemical bands of BiOI@M-MIL are observed clearly, but also a band at 510 cm^{-1} appears owning to bending vibrations of BiOI [36].

The optical properties of BiOI and BiOI@M-MIL were investigated using the diffuse reflectance spectroscopy (DRS) technique. Figure 2 demonstrates the light absorbance of BiOI and BiOI@M-MIL. The light absorbance of BiOI@M-MIL is higher than that of BiOI, which approves of increased absorption of visible light. The band gaps of BiOI and BiOI@M-MIL were calculated using the Kubelka–Munk model. The Kubelka–Munk equation as a function of destruction coefficient (α) and reflectance (R) is defined as follows:

$$\alpha = F(R) = \frac{(1-R)^2}{2R} \quad (1)$$

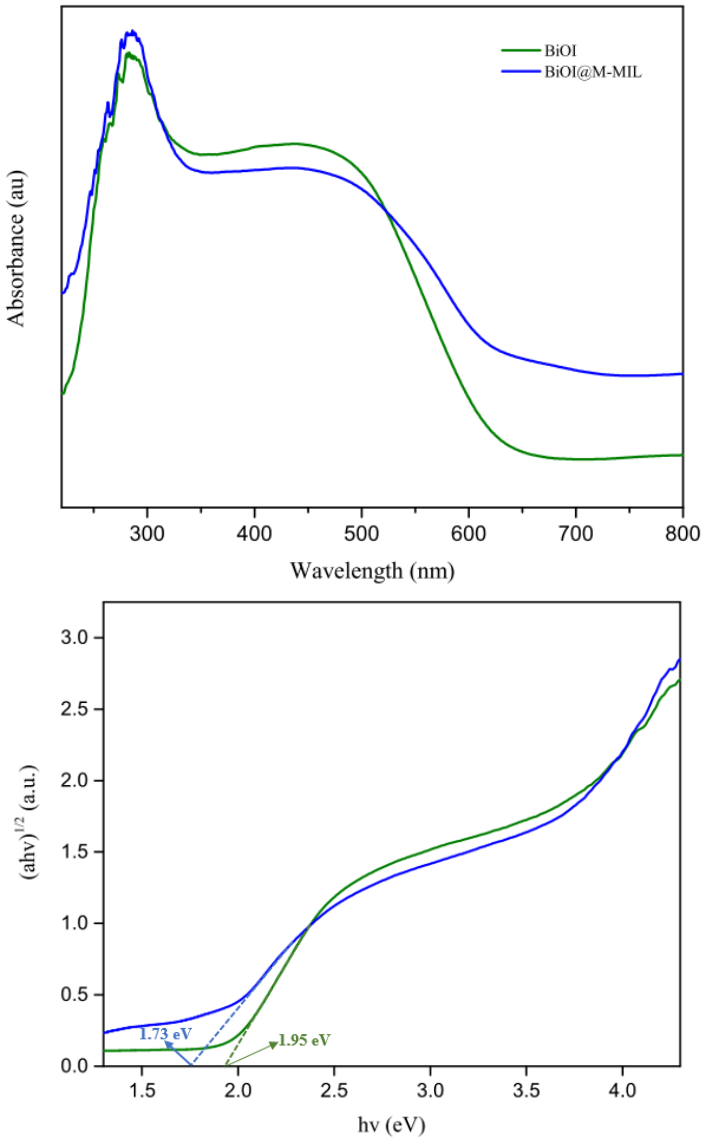


Figure 2. The diffuse reflectance spectroscopy and energy band gap graph for BiOI and BiOI@M-MIL.

The following equation is used for measuring band gap energy (E_g):

$$(\alpha h\nu)^n = A(h\nu - E_g) \quad (2)$$

where $h\nu$, A, and E_g are energy, ratio constant, and band gap energy, respectively. n is considered as 2 or ½ for direct or indirect semiconductors, respectively. As shown in Figure 2, E_{bg} of BiOI and BiOI@M-MIL was calculated at 1.95 and 1.73 eV, respectively. This value was lower than that of BiOI semiconductor. This means that the electrons transport rapidly, and the pollutants degrade quickly [38].

The morphology of MIL-101, M-MIL, BiOI, and BiOI@M-MIL photocatalysts using SEM images are presented in Figure 3a–d. Considering SEM images, M-MIL has an octahedral structure with a rough surface and distinct edges with a size of 1–2 µm, while BiOI possesses a sheet-like structure. Also, BiOI@M-MIL is composed of sheet structures with diameters of about 100–300 nm.

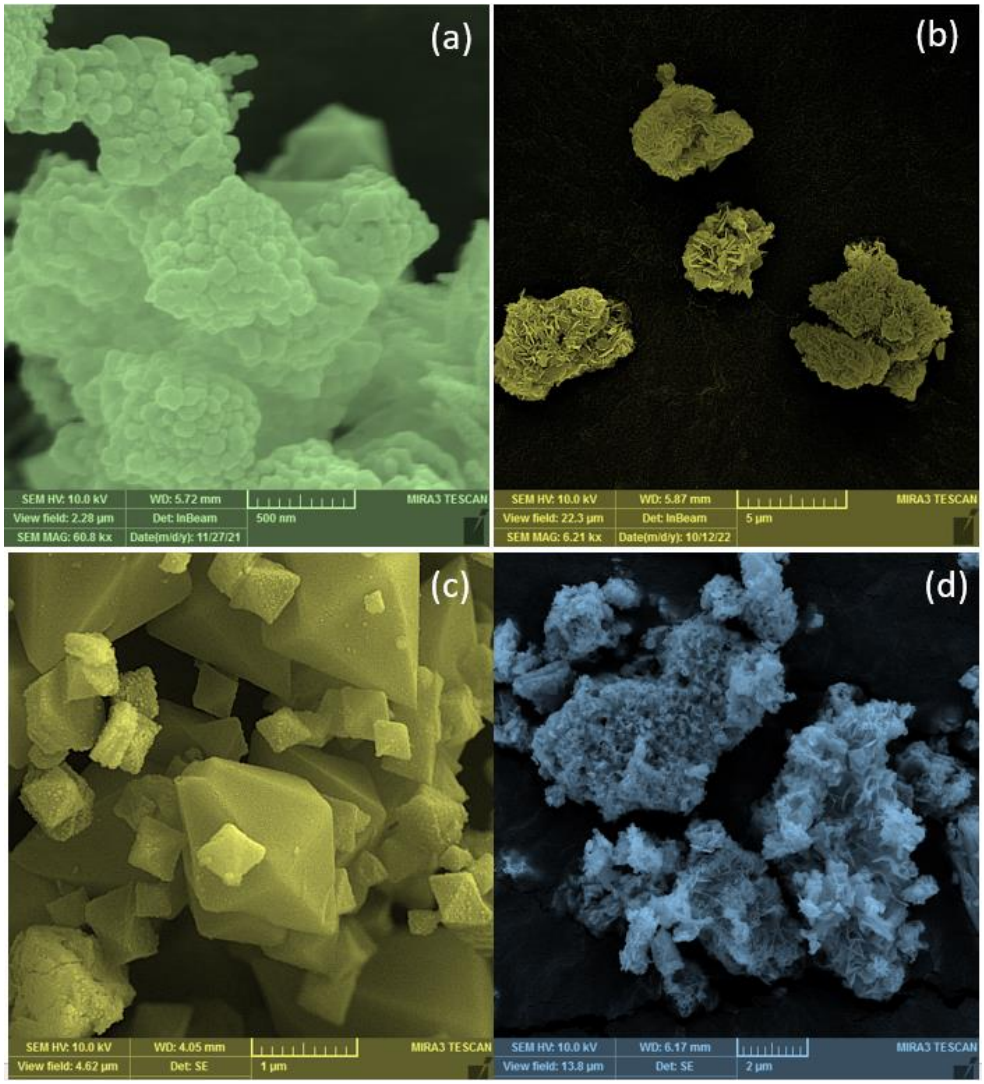


Figure 3. The SEM images of (**a**) M-MIL, (**b**) BiOI, (**c**) MIL-101, and (**d**) BiOI@M-MIL.

2.2. Screening Study

Screening tests were conducted to demonstrate that the integration of modified MIL into BiOI structure produces binary BiOI@M-MIL with enhanced adsorption and photocatalytic performance compared to pristine BiOI. Figure 4 compares the AR14 discoloration by the prepared materials, i.e., BiOI, MMIL, and BiOI@M-MIL. As seen, BiOI@M-MIL shows significant photocatalytic performance compared to pristine BiOI. After 75 min irradiation time, the dye discoloration for BiOI@M-MIL was 95.4%, which was 1.81 times more than 52.7 for BiOI. M-MIL exhibits significant dye removal efficiency, particularly during the initial mixing time. However, this performance diminishes over time, indicating that the dye is primarily adsorbed by M-MIL initially but subsequently desorbs. Figure 4 also shows the photolysis of the AR14, which is negligible (<1%) over 75 min of irradiation time.

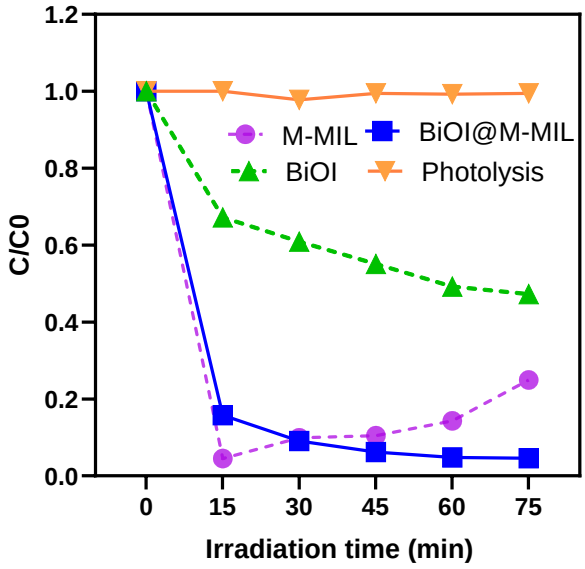


Figure 4. The discoloration performance of M-MIL, BiOI, and BiOI@M-MIL for AR14.

2.3. Parametric Study

AR14 discoloration was examined over a pH range of 4–10, with other parameters set as follows: nanocomposite dose at 0.5 g L^{-1}, AR14 concentration at 25 mg L^{-1}, and photoreaction time of 60 min. As illustrated in Figure 5, dye discoloration through adsorption and photocatalysis was most effective in an acidic environment. The removal efficiency significantly increased from 91.9% to 95.1% as the pH was raised from 4 to 6. However, further increasing the pH from 6 to 10 caused a notable decrease in discoloration efficiency, dropping to approximately 63%. Consequently, subsequent experiments to investigate the role of other operating variables were conducted at the optimal pH of 6.

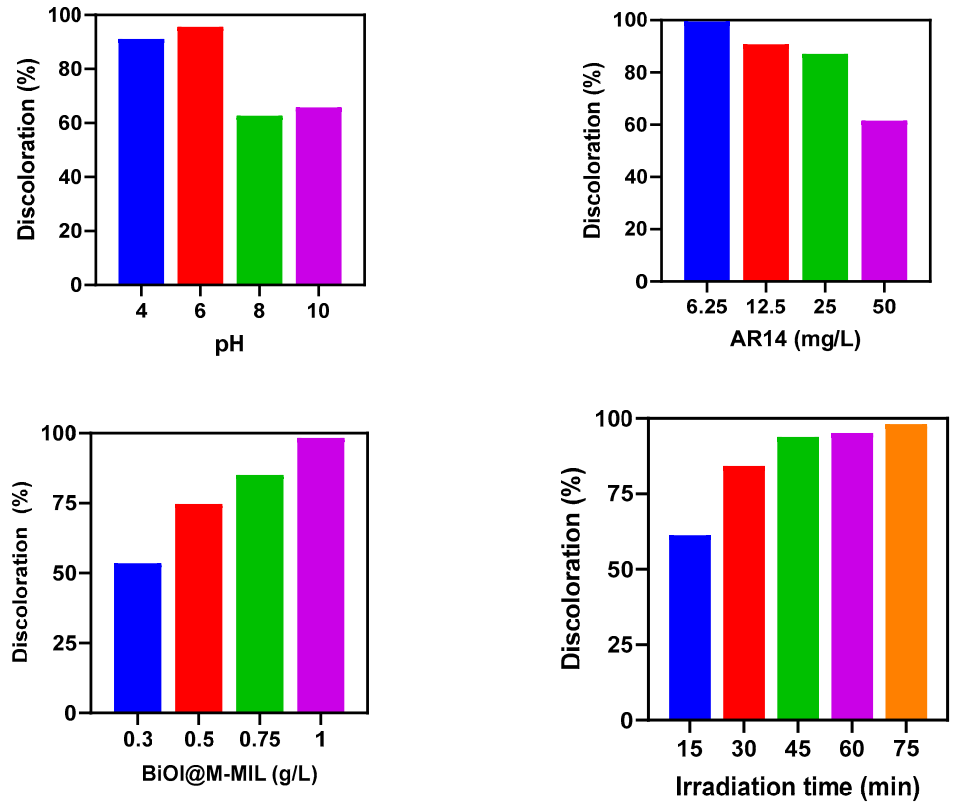


Figure 5. The effect of operating variables on AR14 removal by BiOI@M-MIL.

In this study, the effect of AR14 dye concentration on pollutant discoloration efficiency was surveyed. As shown in Figure 5, with a reduction of AR14 concentration from 50 to 6.25 mg L^{-1}, the efficiency decreased from about 99.4% to about 61.5%, which shows the material has excellent performance in pollutant discoloration, particularly at low concentrations. The role of increased dye concentration in suppressing the photocatalysis and adsorption performance is well documented in earlier works. Increasing AR14 concentration could hinder the light penetration that is essential to radical formation by BiOI@M-MIL. Moreover, the accumulated dye molecules on the surface could interfere with the catalytic performance. According to adsorption theory, the pollutant uptake occurred at specific and limited sorption sites. Consequently, at elevated concentrations, the process is controlled by the limiting free sorption sites of BiOI@M-MIL.

The study indicated that the rate of degradation decreases with initial RhB concentration, which is attributed to the blanket effect developed by the coverage of catalyst active sites [39]. Prasad Sapkota et al. reported 97.33% photodegradation of methylene blue using ZnO–single-walled carbon nanotube composites in 2 h under the visible light spectrum [40]. Similar findings were reported on simultaneous photo/sonocatalytic reduction of AR14 by Fe_3O_4@SiO_2/PAEDTC@MIL-101. In a study, the magnetic Fe_3O_4@SiO_2/PAEDTC@MIL-101 was used for the degradation of AR14 with the maximum removal efficiencies of 100% at 50 mg/L initial concentration of AR14, pH of 5, and 0.5 g/L catalyst mass [41]. The quenching of active sites and the limitation of radical formation have also been reported as mechanisms reducing the photocatalytic degradation of recalcitrant perfluorooctanoic acid (PFOA) by BiOCl/Zn-Al hydrotalcite under UV irradiation [42].

Figure 5 illustrates the effect of BiOI@M-MIL dosage on AR14 discoloration efficiency. A dosage range of 0.3–1.0 g L^{-1} was selected based on preliminary optimization experiments to ensure effective discoloration within a reasonable timeframe. Under constant conditions (dye concentration of 25 mg L^{-1}, pH 6, and reaction time of 60 min), the discoloration efficiency significantly increased from 53.5% to approximately 98.4% as the nanocomposite dosage was raised from 0.3 to 1.0 g L^{-1}. In addition, the discoloration efficiency exceeded 70% for all photocatalyst dosages above 0.5 g L^{-1}.

Higher absorption of the dye molecules and the production of more active radicals increased the dye removal at elevated dosages of BiOI@M-MIL. However, earlier studies have indicated a reduction in process efficiency due to the development of solution turbidity at higher masses, whereas BiOI@M-MIL did not show similar behavior. This could be attributed to the composite taking advantage of its synergistic and catalytic activity [43,44].

The effect of irradiation time on the dye discoloration was evaluated in the 15–75 min. As presented in Figure 5, by increasing the irradiation time, the efficiency increased significantly from 61.3% to 98.1%. This observation can be attributed to the production of more active radicals in the discoloration of AR14 dye over time. Also, by increasing the irradiation time from 45 to 75 min, the discoloration efficiency reached an almost complete removal.

2.4. Photocatalyst Performance in the Real Sample

The catalytic performance of BiOI@M-MIL in real wastewater in the presence of co-current ions was evaluated to understand the potential application of the composite. A sample is taken from the effluent of a secondary sedimentation tank that treats municipal wastewater. After bringing to the lab, the samples were centrifuged to produce a clear solution, spiked with 25 mg L^{-1} AR14 dye, and the pH adjusted to 6. The solution was then treated with a BiOI@M-MIL dosage of 0.5 g L^{-1} for 90 min irradiation time. The discoloration efficiency of AR14 was reduced to 49.3% for real wastewater compared to the full discoloration for control. The interference of co-current compounds in the real matrix led to a reduction in overall reaction performance. Additionally, the accumulation

of intermediate compounds on the photocatalyst surface can hinder its activity by blocking active sites [45,46].

2.5. Durability of BiOI@M-MIL

It is significant to study the photocatalytic activity of BiOI@M-MIL in successive use–reuse cycles to examine its stability and reusability. Hence, the reusability of BiOI@M-MIL was tested under optimized conditions. The results of composite efficiency against AR 14 in five cycles are shown in Figure 6. As seen, the discoloration efficiency decreased by 13.8% after five cycles, demonstrating the high recyclability of BiOI@M-MIL.

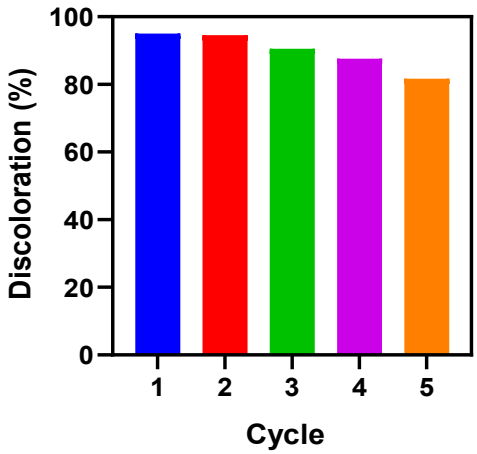


Figure 6. The performance of BiOI@M-MIL for AR14 discoloration in consecutive use–reuse cycles.

2.6. Photocatalytic Discoloration Kinetics

Kinetic studies are important in photocatalytic reactions to determine how the process advances over time. The photocatalytic discoloration of AR14 in different initial dye concentrations of 50, 25, and 12.5 mg L^{-1} was studied in the optimal condition obtained in parametric studies.

The relationship between AR14 concentration and photoreaction time was introduced as a rate constant. To access rate constants of AR14 discoloration, dye removal was evaluated over time and as a function of concentration. Table 1 shows the parameters of pseudo-first-order (PFO) and pseudo-second-order (PSO) kinetic models, including k_{app} and R^2 values. When the initial concentration ranged from 50 to 12.5 mg L^{-1}, the constant rate increased slightly from 0.002 to 0.002 min^{-1} in pseudo-first-order and from 0.01 to 0.02 L mg^{-1} min^{-1} in pseudo-second-order models. The data presented in the table indicate that the R^2 values for the pseudo-second-order kinetic model are consistently higher compared to those for the pseudo-first-order model. This suggests that the discoloration kinetics of AR14 dye is likely controlled by chemisorption.

Table 1. Pseudo-first and pseudo-second-order kinetics parameters for AR14 dye discoloration by BiOI@M-MIL.

Dye Concentration (mg L^{-1})	k_{app} (min^{-1})	R^2 (PFO)	k_{app} (L mg^{-1} min^{-1})	R^2 (PSO)
50.0	0.002	0.94	0.01	0.98
25.0	0.002	0.91	0.01	0.98
12.5	0.002	0.94	0.02	0.99

2.7. Radical Trapping Experiments

The scavenger experiments were conducted to obtain the most active species in the discoloration of AR14 dye. KI, IPA, $AgNO_3$, and BQ were used to assess the role of active species such as holes, hydroxyl radicals, electrons, and O_2^- in AR14 discoloration [47]. As seen in Figure 7, the discoloration efficiency of BiOI@M-MIL was decreased from 94% to 76, 88, 90, and 91% by adding BQ, IPA, $AgNO_3$, and KI, respectively. A significant loss after adding BQ indicated that the superoxide radicals, plays an important role in the photocatalytic process.

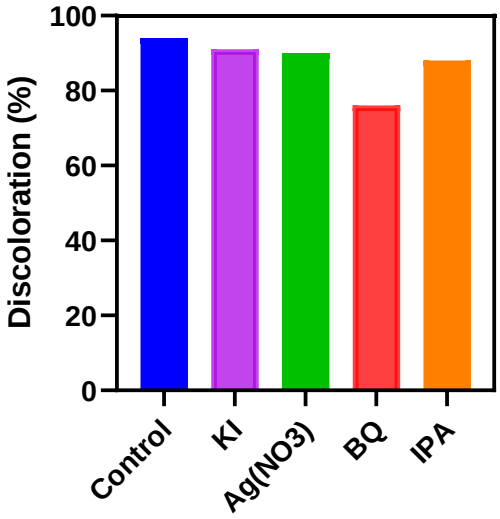


Figure 7. The performance of BiOI@M-MIL for AR14 discoloration in the presence of radical scavengers.

2.8. Adsorption Study

In catalysis, adsorption plays a synergistic role that can significantly enhance the overall efficiency of the process. Adsorption not only increases the AR14 concentration on the catalyst surface but also increases their availability for subsequent catalytic degradation. Herein, dye adsorption onto BiOI@M-MIL was investigated after equilibrium was achieved. The isotherm models were fitted, and the results are presented in Figure 8. Isotherm parameters and the related correlation coefficients are presented in Table 2. As observed, the Sips model exhibits the best correlation with the experimental data. This model is an empirical equation that combines the theoretical Langmuir and empirical Freundlich models to provide a suitable description of adsorption on heterogeneous surfaces [48]. Based on this observation, the adsorption of AR14 likely occurs in multiple layers on the heterogenous structure composed of BiOI and modified MIL. The highest adsorption capacities of BiOI@M-MIL were determined to be 45.32 mg g^{-1} and 32.2 mg g^{-1} according to the Sips and Langmuir models, respectively.

Table 2. Non-linear isotherm models [49] fitted on equilibrium data for AR14 removal by BiOI@M-MIL.

Model	Linear Form	Parameter	Value
Langmuir	$q_e = \frac{Q_0 K_L C_e}{1+ K_L C_e}$	q_{max} (mg/g)	32.2
		K_L (L/mg)	0.35
		R^2	0.98
		R^2_{adj}	0.98
		RSS	7.69

Table 2. *Cont.*

Model	Linear Form	Parameter	Value
Freundlich	$q_e = K_f C_e^{1/n}$	K_F $mg/g(L/mg)^{1/n}$	11.3
		n	3.4
		R^2	0.99
		R^2_{adj}	0.99
		RSS	4.00
Temkin	$q_e = \frac{RT}{B} \ln(A_T C_e)$	k_t (L/mg)	4.99
		B_1	6.00
		R^2	0.99
		R^2_{adj}	0.99
		RSS	0.7
Redlich–Peterson	$q_e = \frac{K_{RP} C_e}{1 + a_{RP} C_e^g}$	k_{RP} (L g^{-1})	24.01
		a_{RP} (mg L^{-1})$^{-bRP}$	1.41
		b_{RP}	0.81
		R^2	0.99
		R^2_{adj}	0.99
		RSS	0.4
Sips	$q_e = \frac{q_{ms} K_s C_e^{ms}}{1 + K_s C_e^{ms}}$	q_{ms} (mg g^{-1})	45.32
		K_S (L mg^{-1})^{ms}	0.28
		m_s	0.57
		R^2	0.99
		R^2_{Adj}	0.99
		RSS	0.27

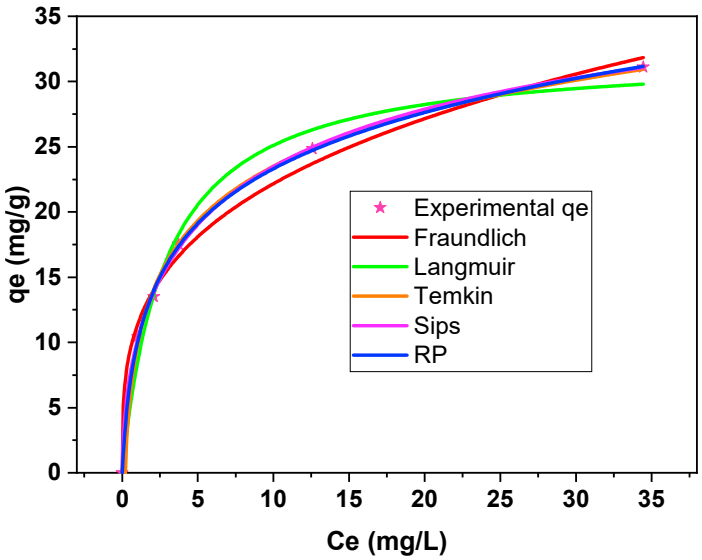


Figure 8. Non-linear isotherm models fitted on equilibrium data for AR14 removal by BiOI@M-MIL.

2.9. Comparison of Photocatalytic Performance by BiOI-Based Photocatalysts

The comparison of various BiOI-based photocatalysts' performance for discoloration of azo dyes is presented in Table 3. As seen, BiOI@M-MIL could be suggested as a promising catalyst not only for its good removal efficiency but also for its photo reactivity under a low-energy light source that complies with sustainable principles [50]. Also, the discoloration efficiency of BiOI@M-MIL photocatalyst was enhanced compared to commercial photocatalysts such as P25 or commercial TiO_2. For instance, the degradation of AR14 dye using amino-functionalized CeO_2 (ceria) was as high as (95.6%) in only 1 h of irradiation due to an improvement of the photodegradation rate [51]. In the present study, the efficiency of

AR14 using BiOI@M-MIL was about 94% after 1 h irradiation, while only 15% of AR14 was degraded over P25, indicating the industrial potential of BiOI@M-MIL photocatalyst.

Table 3. Comparison of photocatalytic performance of BiOI-based structures.

Photocatalyst	Dose (g L^{-1})	Concentration (mg L^{-1})	Pollutant	Irradiation Time (min)	Light Source	η%	Reference
BiOBr/BiOI	0.4	15	RhB	40	>420 nm	100	[52]
BiOBr/BiOI	0.4	40	Tetracycline	50	>420 nm	83	[52]
Fe/Zn–BiOI	0.4	10	Tetracycline	60	xenon lamp (380–900 nm)	83	[53]
SnO_{2-x}/BiOI	-	-	Tetracycline	60	LED lamp	80	[54]
BiOI@M-MIL	0.5	25	AR14	75	LED lamp	100	Our work

3. Experimental

3.1. Chemicals, Materials Synthesis Protocols, and Characterization Instruments

The materials used for the synthesis of MIL-101, BiOI, and the composite, as well as the synthesis protocols, are presented in the Supplementary Materials. The supporting documents also listed the instruments used for material characterization and the module of LED light irradiation. Figure 9 shows the schematic diagram for materials preparation and experimental study for dye removal.

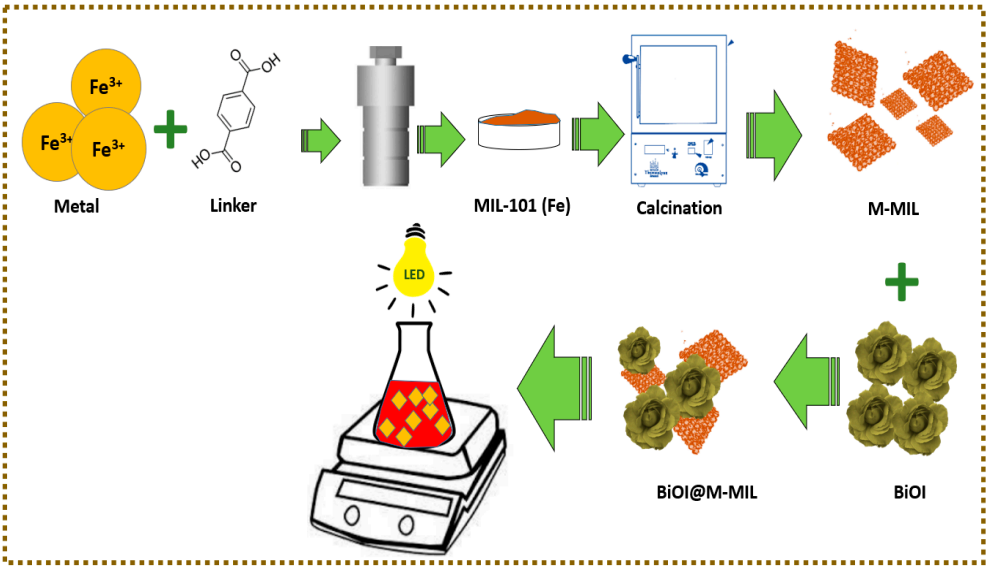


Figure 9. The schematic flow diagram of materials preparation and experimental study.

3.2. Photocatalytic Experiments

The photocatalytic activity of the prepared BiOI-modified MIL-101 (M-MIL) and BiOI@M-MIL was conducted by discoloration of AR14 under visible light irradiation at room temperature. In a typical process, the photocatalyst powder was poured into solutions of AR14 with a certain initial concentration. The surface of the suspension was 2 cm away from the LED lamp. 5 mL of the suspension was sampled and separated by centrifugation after the desired irradiation time. The concentration of AR14 was obtained by measuring the absorbance in the maximum absorption wavelength of AR14 at 515 nm. The discoloration efficiency (DE%) was calculated by the following equation:

$$\mathrm{DE}\ (\%) = \frac{(C_0 - C_t)}{C_0} \times 100 \quad (3)$$

where C_0 and C_t are the concentrations at the initial and time *t*, respectively.

One factor-at-a-time approach experiment was conducted to study the effects of pH (4–10), reaction time (15–75 min), dye concentration (6.25–50.00 mg L^{-1}), and nanocomposite dosage (0.3–1.0 g L^{-1}).

3.3. Kinetic Studies

Kinetic studies are important in photocatalytic reactions to determine how the process advances over time. In this study, the primary focus was to monitor the discoloration of the parent dye molecule using its characteristic absorbance peak. While this approach provides valuable kinetic information, we acknowledge that discoloration intermediates or products may also exhibit absorbance in the same or nearby regions of the spectrum. To address this concern, we conducted a detailed analysis of the UV–Vis spectra throughout the discoloration process. The evolution of the spectra indicates that the characteristic absorbance peak of the parent dye decreases without the appearance of significant new peaks, suggesting that the intermediates formed either do not absorb significantly in the monitored region or are present in negligible concentrations. The photocatalytic discoloration of AR14 in different initial dye concentrations of 50, 25, and 12.5 mg L^{-1} was studied in the optimal condition obtained in parametric studies. Two common kinetic models of pseudo-first (Equation (4)) and pseudo-second orders (Equation (5)) were fit on experimental data [55].

$$ln\frac{C_t}{C_0} = -k_{app} \times t \quad (4)$$

$$\frac{1}{C_t} - \frac{1}{C_0} = k_{app} \times t \quad (5)$$

where k_{app} is the rate constant for the pseudo-first (min^{-1}) and the pseudo-second (L mg^{-1} min^{-1}) orders reactions. C_0 and C_t, are the concentration of AR14 dye at the initial (t = 0) and the concentration at the time of *t*, respectively. In this study, the discoloration of the dye was investigated by pseudo-first-order or pseudo-second-order kinetic models. This assumption is based on experimental conditions, where the concentration of the dye is much lower than that of the photocatalyst dosage. Under these conditions, the concentrations of the latter species are effectively constant throughout the reaction, allowing the reaction rate to depend primarily on the dye concentration.

3.4. Reusability Experiments

The reusability of BiOI@M-MIL for the discoloration of AR14 under LED light irradiation was evaluated in five cycles at optimal conditions. After each cycle, the photocatalyst was centrifuged and washed toughly with deionized water and one time with ethanol and dried at 80 °C. The material is then used for the next photocatalysis cycle. The efficiency of AR14 removal after each cycle =was measured to assess the performance of the exhausted material.

3.5. Mechanism of AR14 Discoloration

The main species involved in the photocatalytic discoloration of dye was identified using radical scavengers. Scavengers including KI (trapper for h^+), IPA (trapper for $^{\circ}OH$), $AgNO_3$ (trapper for e^-), and BQ (trapper for $O_2^{\cdot-}$) were used to distinguish active species in the process. 2 mmol L^{-1} of scavengers was separately introduced into the reaction vessel containing AR14 dye. A sample without a scavenger was considered as a control. Finally, the effect of each scavenger on the AR14 removal was determined to determine the radical that mostly controls the discoloration performance.

3.6. Adsorption Equilibrium Study

To understand the adsorptive behavior of BiOI@M-MIL for AR14, a series of experiments were conducted in the absence of light irradiation. After the adsorption was completed within 60 min, the equilibrium data were analyzed using different non-linear isotherm models to elucidate the adsorption capacities and characteristics.

4. Conclusions

Herein, we have developed a promising binary catalyst made up of modified MIL-101 and BiOI. The materials were fully characterized for structural and optical properties. α-Fe_2O_3 derived MIL has a uniform octahedral structure of 1–2 µm, which was integrated with one-dimensional bismuth oxyiodide (BiOI). BiOI@M-MIL exhibited superior photocatalytic performance compared to pristine semiconductor BiOI. These exceptional properties were demonstrated through optical characterization and experimental studies. A model azo dye Acid red 14 (AR14) was used for the experimental setting. The catalyst was simply activated by a visible-light LED lamp with a power output of 5 W that provides a low-cost and sustainable source of energy. The effect of catalyst dose, pH, dye concentration, and contact time was investigated on AR 14 discoloration. Almost a complete AR 14 removal was achieved when operating variables were adjusted at their optimal levels. Dye adsorption tests indicated that they take advantage of synergistic adsorption and photocatalytic activities. Radical trapping analysis demonstrated the crucial role of $O_2^{\cdot}$ in the discoloration of AR14. A good reusability for the catalyst was observed after five consecutive cycles of use–reuse.

Supplementary Materials: The following supporting information can be downloaded at: https://www.mdpi.com/article/10.3390/catal15010026/s1, Chemicals and reagents; Synthesis of MIL-101 and M-MIL; Synthesis of BiOI@ M-MIL; Characterization; Module of LED light irradiation. See Refs [56,57].

Author Contributions: Methodology, E.K.G.; Validation, M.B.; Formal analysis, S.A.M.; Data curation, M.S. (Masoomeh Shafaee); Writing—original draft, M.S. (Mahmoud Shams); Writing—review & editing, N.E.H. and S.R.; Visualization, A.D.; Supervision, S.R. All authors have read and agreed to the published version of the manuscript.

Funding: To MUMS for the support under Grant # 992391.

Data Availability Statement: The original contributions presented in this study are included in the article/Supplementary Materials. Further inquiries can be directed to the corresponding author.

Conflicts of Interest: The authors declare no conflict of interest.

References

1. Sharma, S.; Bhattacharya, A. Drinking water contamination and treatment techniques. *Appl. Water Sci.* **2017**, *7*, 1043–1067. [CrossRef]
2. Fard, M.A.; Barkdoll, B. Effects of oxalate and persulfate addition to Electrofenton and Electrofenton-Fenton processes for oxidation of Ketoprofen: Determination of reactive species and mass balance analysis. *Electrochim. Acta* **2018**, *265*, 209–220. [CrossRef]
3. Ma, B.; Tian, G.; Kong, L. Spatial-temporal characteristics of China's industrial wastewater discharge at different scales. *Environ. Sci. Pollut. Res.* **2020**, *27*, 8103–8118. [CrossRef] [PubMed]
4. Kishor, R.; Purchase, D.; Saratale, G.D.; Saratale, R.G.; Ferreira, L.F.R.; Bilal, M.; Chandra, R.; Bharagava, R.N. Ecotoxicological and health concerns of persistent coloring pollutants of textile industry wastewater and treatment approaches for environmental safety. *J. Environ. Chem. Eng.* **2021**, *9*, 105012. [CrossRef]
5. Berradi, M.; Hsissou, R.; Khudhair, M.; Assouag, M.; Cherkaoui, O.; El Bachiri, A.; El Harfi, A. Textile finishing dyes and their impact on aquatic environs. *Heliyon* **2019**, *5*, e02711. [CrossRef] [PubMed]

6. Bahadur, N.; Bhargava, N. Novel pilot scale photocatalytic treatment of textile & dyeing industry wastewater to achieve process water quality and enabling zero liquid discharge. *J. Water Process. Eng.* **2019**, *32*, 100934. [CrossRef]
7. Samarghandi, M.R.; Dargahi, A.; Nasab, H.Z.; Ghahramani, E.; Salehi, S. Degradation of azo dye Acid Red 14 (AR14) from aqueous solution using H_2O_2/nZVI and $S_2O_8^{2-}$/nZVI processes in the presence of UV irradiation. *Water Environ. Res.* **2020**, *92*, 1173–1183. [CrossRef]
8. Jabbar, Z.H.; Graimed, B.H. Recent developments in industrial organic degradation via semiconductor heterojunctions and the parameters affecting the photocatalytic process: A review study. *J. Water Process. Eng.* **2022**, *47*, 102671. [CrossRef]
9. Zhao, L.; Guo, R.; Sun, Q.; Lan, J.; Li, H. Interaction between azo dye Acid Red 14 and pepsin by multispectral methods and docking studies. *Luminescence* **2017**, *32*, 1123–1130. [CrossRef]
10. Idel-Aouad, R.; Valiente, M.; Gutiérrez-Bouzán, C.; Vilaseca, M.; Yaacoubi, A.; Tanouti, B.; López-Mesas, M. Relevance of Toxicity Assessment in Wastewater Treatments: Case Study—Four Fenton Processes Applied to the Mineralization of C.I. Acid Red 14. *J. Anal. Methods Chem.* **2015**, *2015*, 945489. [CrossRef] [PubMed]
11. Oveisi, M.; Asli, M.A.; Mahmoodi, N.M. Carbon nanotube based metal-organic framework nanocomposites: Synthesis and their photocatalytic activity for decolorization of colored wastewater. *Inorganica Chim. Acta* **2018**, *487*, 169–176. [CrossRef]
12. Foteinis, S.; Chatzisymeon, E. Heterogeneous Photocatalysis for Water Purification. In *Nanostructured Photocatal*; Elsevier: Amsterdam, The Netherlands, 2020; pp. 75–97. [CrossRef]
13. Nosaka, Y.; Nosaka, A.Y. Generation and Detection of Reactive Oxygen Species in Photocatalysis. *Chem. Rev.* **2017**, *117*, 11302–11336. [CrossRef] [PubMed]
14. Cai, G.; Yan, P.; Zhang, L.; Zhou, H.-C.; Jiang, H.-L. Metal–Organic Framework-Based Hierarchically Porous Materials: Synthesis and Applications. *Chem. Rev.* **2021**, *121*, 12278–12326. [CrossRef] [PubMed]
15. Chen, X.; Peng, X.; Jiang, L.; Yuan, X.; Yu, H.; Wang, H.; Zhang, J.; Xia, Q. Recent advances in titanium metal–organic frameworks and their derived materials: Features, fabrication, and photocatalytic applications. *Chem. Eng. J.* **2020**, *395*, 125080. [CrossRef]
16. Li, Z.; Liu, X.; Jin, W.; Hu, Q.; Zhao, Y. Adsorption behavior of arsenicals on MIL-101(Fe): The role of arsenic chemical structures. *J. Colloid Interface Sci.* **2019**, *554*, 692–704. [CrossRef]
17. Baziar, M.; Zakeri, H.R.; Askari, S.G.; Nejad, Z.D.; Shams, M.; Anastopoulos, I.; Giannakoudakis, D.A.; Lima, E.C. Metal-organic and Zeolitic imidazole frameworks as cationic dye adsorbents: Physicochemical optimizations by parametric modeling and kinetic studies. *J. Mol. Liq.* **2021**, *332*, 115832. [CrossRef]
18. Reddy, C.V.; Reddy, K.R.; Harish, V.; Shim, J.; Shankar, M.; Shetti, N.P.; Aminabhavi, T.M. Metal-organic frameworks (MOFs)-based efficient heterogeneous photocatalysts: Synthesis, properties and its applications in photocatalytic hydrogen generation, CO_2 reduction and photodegradation of organic dyes. *Int. J. Hydrogen Energy* **2019**, *45*, 7656–7679. [CrossRef]
19. Yang, F.; Du, M.; Yin, K.; Qiu, Z.; Zhao, J.; Liu, C.; Zhang, G.; Gao, Y.; Pang, H. Applications of Metal-Organic Frameworks in Water Treatment: A Review. *Small* **2021**, *18*, 2105715. [CrossRef]
20. Li, Z.; Huang, G.; Liu, K.; Tang, X.; Peng, Q.; Huang, J.; Ao, M.; Zhang, G. Hierarchical BiOX (X = Cl, Br, I) microrods derived from Bismuth-MOFs: In situ synthesis, photocatalytic activity and mechanism. *J. Clean. Prod.* **2020**, *272*, 122892. [CrossRef]
21. Liu, Y.; Xu, J.; Wang, L.; Zhang, H.; Xu, P.; Duan, X.; Sun, H.; Wang, S. Three-Dimensional BiOI/BiOX (X = Cl or Br) Nanohybrids for Enhanced Visible-Light Photocatalytic Activity. *Nanomaterials* **2017**, *7*, 64. [CrossRef] [PubMed]
22. Meng, X.; Zhang, Z. New insight into BiOX (X = Cl, Br, and I) hierarchical microspheres in photocatalysis. *Mater. Lett.* **2018**, *225*, 152–156. [CrossRef]
23. Wang, Z.; Chen, M.; Huang, D.; Zeng, G.; Xu, P.; Zhou, C.; Lai, C.; Wang, H.; Cheng, M.; Wang, W. Multiply structural optimized strategies for bismuth oxyhalide photocatalysis and their environmental application. *Chem. Eng. J.* **2019**, *374*, 1025–1045. [CrossRef]
24. Arumugam, M.; Choi, M.Y. Recent progress on bismuth oxyiodide (BiOI) photocatalyst for environmental remediation. *J. Ind. Eng. Chem.* **2019**, *81*, 237–268. [CrossRef]
25. Wei, Z.; Liu, J.; Fang, W.; Qin, Z.; Jiang, Z.; Shangguan, W. A visible-light driven novel layered perovskite oxyhalide Bi_4MO_8X (M = Nb, Ta; X = Cl, Br) constructed using BiOX (X = Cl, Br) for enhanced photocatalytic hydrogen evolution. *Catal. Sci. Technol.* **2018**, *8*, 3774–3784. [CrossRef]
26. Jiang, W.; Li, Z.; Liu, C.; Wang, D.; Yan, G.; Liu, B.; Che, G. Enhanced visible-light-induced photocatalytic degradation of tetracycline using BiOI/MIL-125(Ti) composite photocatalyst. *J. Alloys Compd.* **2021**, *854*, 157166. [CrossRef]
27. Khasevani, S.G.; Gholami, M. Engineering a highly dispersed core@shell structure for efficient photocatalysis: A case study of ternary novel BiOI@MIL-88A(Fe)@g-C_3N_4 nanocomposite. *Mater. Res. Bull.* **2018**, *106*, 93–102. [CrossRef]
28. Meng, L.; Zhao, C.; Wang, T.; Chu, H.; Wang, C.-C. Efficient ciprofloxacin removal over Z-scheme ZIF-67/V-$BiOIO_3$ heterojunctions: Insight into synergistic effect between adsorption and photocatalysis. *Sep. Purif. Technol.* **2023**, *313*, 123511. [CrossRef]
29. Mukherjee, D.; Van der Bruggen, B.; Mandal, B. Advancements in visible light responsive MOF composites for photocatalytic decontamination of textile wastewater: A review. *Chemosphere* **2022**, *295*, 133835. [CrossRef]

30. Islam, M.J.; Kim, H.K.; Reddy, D.A.; Kim, Y.; Ma, R.; Baek, H.; Kim, J.; Kim, T.K. Hierarchical BiOI nanostructures supported on a metal organic framework as efficient photocatalysts for degradation of organic pollutants in water. *Dalton Trans.* **2017**, *46*, 6013–6023. [CrossRef] [PubMed]
31. Liang, Q.; Cui, S.; Jin, J.; Liu, C.; Xu, S.; Yao, C.; Li, Z. Fabrication of BiOI@UIO-66(NH_2)@g-C_3N_4 ternary Z-scheme heterojunction with enhanced visible-light photocatalytic activity. *Appl. Surf. Sci.* **2018**, *456*, 899–907. [CrossRef]
32. Dai, D.; Qiu, J.; Zhang, L.; Ma, H.; Yao, J. Amino-functionalized Ti-metal-organic framework decorated BiOI sphere for simultaneous elimination of Cr(VI) and tetracycline. *J. Colloid Interface Sci.* **2021**, *607*, 933–941. [CrossRef] [PubMed]
33. Khasevani, S.G.; Nikjoo, D.; Chaxel, C.; Umeki, K.; Sarmad, S.; Mikkola, J.-P.; Concina, I. Empowering Adsorption and Photocatalytic Degradation of Ciprofloxacin on BiOI Composites: A Material-by-Design Investigation. *ACS Omega* **2023**, *8*, 44044–44056. [CrossRef] [PubMed]
34. Lei, Y.; Wang, G.; Song, S.; Fan, W.; Pang, M.; Tang, J.; Zhang, H. Room temperature, template-free synthesis of BiOI hierarchical structures: Visible-light photocatalytic and electrochemical hydrogen storage properties. *Dalton Trans.* **2010**, *39*, 3273–3278. [CrossRef] [PubMed]
35. Nourzad, M.; Dehghan, A.; Niazi, Z.; Giannakoudakis, D.A.; Afsharnia, M.; Barczak, M.; Anastopoulos, I.; Triantafyllidis, K.S.; Shams, M. Low power photo-assisted catalytic degradation of azo dyes using 1-D BiOI: Optimization of the key physicochemical features. *Catal. Commun.* **2022**, *174*, 106567. [CrossRef]
36. Tong, Y.-H.; Wu, Y.-Z.; Xu, Z.-L.; Luo, L.-H.; Xu, S.-J. Photocatalytic self-cleaning EVAL membrane by incorporating bio-inspired functionalized MIL-101(Fe) for dye/salt separation. *Chem. Eng. J.* **2022**, *444*, 136507. [CrossRef]
37. Ma, Y.; Li, M.; Jiang, J.; Li, T.; Wang, X.; Song, Y.; Dong, S. In-situ prepared MIL-53(Fe)/BiOI photocatalyst for efficient degradation of tetracycline under visible-light driven photo-Fenton system: Investigation of performance and mechanism. *J. Alloy. Compd.* **2021**, *870*, 159524. [CrossRef]
38. Jin, Y.; Mi, X.; Qian, J.; Ma, N.; Dai, W. Modular Construction of an MIL-101(Fe)@MIL-100(Fe) Dual-Compartment Nanoreactor and Its Boosted Photocatalytic Activity toward Tetracycline. *ACS Appl. Mater. Interfaces* **2022**, *14*, 48285–48295. [CrossRef] [PubMed]
39. Dehghan, A.; Dehghani, M.H.; Nabizadeh, R.; Ramezanian, N.; Alimohammadi, M.; Najafpoor, A.A. Adsorption and visible-light photocatalytic degradation of tetracycline hydrochloride from aqueous solutions using 3D hierarchical mesoporous BiOI: Synthesis and characterization, process optimization, adsorption and degradation modeling. *Chem. Eng. Res. Des.* **2018**, *129*, 217–230. [CrossRef]
40. Sapkota, K.P.; Lee, I.; Hanif, A.; Islam, A.; Akter, J.; Hahn, J.R. Enhanced Visible-Light Photocatalysis of Nanocomposites of Copper Oxide and Single-Walled Carbon Nanotubes for the Degradation of Methylene Blue. *Catalysts* **2020**, *10*, 297. [CrossRef]
41. Al-Hawary, S.I.S.; Rahimpoor, R.; Rahmani, A.; Romero-Parra, R.M.; Ramírez-Coronel, A.A.; Alhachami, F.R.; Mengelizadeh, N.; Balarak, D. Enhanced Sonophotocatalytic Degradation of Acid Red 14 Using Fe_3O_4@SiO_2/PAEDTC@MIL-101 (Fe) Based on Metal-Organic Framework. *Catalysts* **2023**, *13*, 411. [CrossRef]
42. Nezamzadeh-Ejhieh, A.; Shams-Ghahfarokhi, Z. Photodegradation of Methyl Green by Nickel-Dimethylglyoxime/ZSM-5 Zeolite as a Heterogeneous Catalyst. *J. Chem.* **2012**, *2013*, 104093. [CrossRef]
43. Sakthivel, S.; Neppolian, B.; Shankar, M.; Arabindoo, B.; Palanichamy, M.; Murugesan, V. Solar photocatalytic degradation of azo dye: Comparison of photocatalytic efficiency of ZnO and TiO_2. *Sol. Energy Mater. Sol. Cells* **2002**, *77*, 65–82. [CrossRef]
44. Al-Musawi, T.J.; Rajiv, P.; Mengelizadeh, N.; Mohammed, I.A.; Balarak, D. Development of sonophotocatalytic process for degradation of acid orange 7 dye by using titanium dioxide nanoparticles/graphene oxide nanocomposite as a catalyst. *J. Environ. Manag.* **2021**, *292*, 112777. [CrossRef]
45. Habibi, M.H.; Hassanzadeh, A.; Mahdavi, S. The effect of operational parameters on the photocatalytic degradation of three textile azo dyes in aqueous TiO_2 suspensions. *J. Photochem. Photobiol. A Chem.* **2005**, *172*, 89–96. [CrossRef]
46. Bandala, E.R.; Peláez, M.A.; García-López, A.J.; Salgado, M.d.J.; Moeller, G. Photocatalytic decolourisation of synthetic and real textile wastewater containing benzidine-based azo dyes. *Chem. Eng. Process. Process. Intensif.* **2008**, *47*, 169–176. [CrossRef]
47. Olama, N.; Dehghani, M.; Malakootian, M. The removal of amoxicillin from aquatic solutions using the TiO_2/UV-C nanophotocatalytic method doped with trivalent iron. *Appl. Water Sci.* **2018**, *8*, 97. [CrossRef]
48. Haghighat, G.A.; Gholikandi, G.B.; Mirabi, M.; Shams, M. Photocatalytic removal of crystal violet by C–MIL–53(Fe)@BiOI heterojunction: Process modeling and optimization. *J. Photochem. Photobiol. A Chem.* **2024**, *449*, 115342. [CrossRef]
49. Mittal, V. Polymers from Renewable Resources. In *Renewable Polymers: Synthesis, Processing, and Technology*; Wiley: Hoboken, NJ, USA, 2011; pp. 1–22. [CrossRef]
50. He, L.; Dong, Y.; Zheng, Y.; Jia, Q.; Shan, S.; Zhang, Y. A novel magnetic MIL-101(Fe)/TiO_2 composite for photo degradation of tetracycline under solar light. *J. Hazard. Mater.* **2019**, *361*, 85–94. [CrossRef]
51. Hao, S.; Hou, J.; Aprea, P.; Deng, H. Amino-functionalized ceria with enhanced daylight photocatalytic efficiency. *Ceram. Int.* **2016**, *42*, 7440–7446. [CrossRef]

52. Lin, L.; Huang, M.; Long, L.; Sun, Z.; Zheng, W.; Chen, D. Fabrication of a three-dimensional BiOBr/BiOI photocatalyst with enhanced visible light photocatalytic performance. *Ceram. Int.* **2014**, *40*, 11493–11501. [CrossRef]
53. Talreja, N.; Afreen, S.; Ashfaq, M.; Chauhan, D.; Mera, A.C.; Rodríguez, C.; Mangalaraja, R. Bimetal (Fe/Zn) doped BiOI photocatalyst: An effective photodegradation of tetracycline and bacteria. *Chemosphere* **2021**, *280*, 130803. [CrossRef] [PubMed]
54. Wang, C.; Li, Y.; Yang, L.; Wang, H.; Liu, J.; Liu, J.; Song, Z.; Huang, L. Enhanced photocatalytic antibacterial and degradation performance by n-p type 0D/2D SnO_2-x/BiOI photocatalyst under LED light. *Chem. Eng. J.* **2021**, *411*, 128505. [CrossRef]
55. Niazi, Z.; Goharshadi, E.K.; Mashreghi, M.; Namayandeh Jorabchi, M. Highly efficient solar photocatalytic degradation of a textile dye by TiO_2/graphene quantum dots nanocomposite. *Photochem. Photobiol. Sci.* **2021**, *20*, 87–99. [CrossRef] [PubMed]
56. Li, W.; Wu, X.; Li, S.; Tang, W.; Chen, Y. Magnetic porous Fe3O4/carbon octahedra derived from iron-based metal-organic framework as heterogeneous Fenton-like catalyst. *Appl. Surf. Sci.* **2018**, *436*, 252–262. [CrossRef]
57. Fattahi, M.; Niazi, Z.; Esmaeili, F.; Mohammadi, A.A.; Shams, M.; Nguyen Le, B. Boosting the adsorptive and photocatalytic performance of MIL-101(Fe) against methylene blue dye through a thermal post-synthesis modification. *Sci. Rep.* **2023**, *13*, 14502. [CrossRef] [PubMed]

Disclaimer/Publisher's Note: The statements, opinions and data contained in all publications are solely those of the individual author(s) and contributor(s) and not of MDPI and/or the editor(s). MDPI and/or the editor(s) disclaim responsibility for any injury to people or property resulting from any ideas, methods, instructions or products referred to in the content.